A New Rock Salt Constitutive Model with Back Stress and Drag Stress Hardening

Benjamin Reedlunn

Sandia National Laboratories, P.O. Box 5800, Albuquerque, NM 87112, USA

breedlu@sandia.gov

ABSTRACT: This paper presents a new, largely phenomenological, model for rock salt that includes branches for pressure solution and dislocation glide viscoplasticity. The dislocation glide branch utilizes back stress hardening for heterogeneously distributed dislocations and drag stress hardening for uniformly distributed dislocations. By transitioning between pressure solution at low strain rates, back stress dominated hardening at low to medium strain rates, and drag stress dominated hardening at high strain rates, a single model calibration can capture salt's behavior over strain rates ranging from 10^{-12} to 10^{-4} 1/s. The same model calibration can also simulate the Bauschinger effect (and reverse creep). Although room for improvement exists, the model's elegant formulation can represent an assortment of damage-free behaviors.

1 Introduction

Rock salt constitutive models are used to simulate the evolution of mines, boreholes, storage caverns for gases and liquids, and nuclear waste repositories in rock salt formations. A wide variety of thermomechanical constitutive models have been proposed for rock salt, yet even the damage-free thermoviscoplastic behavior remains difficult to capture. The Munson-Dawson model (Reedlunn 2018), for example, can be calibrated against damage-free constant stress tests with low to medium steady-state strain rates (10^{-12} to 10^{-8} 1/s), but such a calibration fails to represent damage-free constant strain rate tests at high strain rates (10^{-6} to 10^{-4} 1/s). Capturing the damage-free mechanical behavior at these high strain rates is important because high strain rates are frequently used to characterize the mechanical behavior of damaged salt (salt with micro-cracks). A constitutive model must first adequately capture the damage-free behavior before attempting to represent how damage degrades salt's strength.

This paper presents a new model for the damage-free behavior of salt. Section 2 defines the model formulation, Section 3 briefly discusses the formulation, Section 4 details four model calibrations, Section 5 validates the model against an observation of the Bauschinger effect, and Section 6 provides a short summary.

2 Model Formulation

Several preliminaries bear mentioning before defining the model formulation. First, compressive strains and stresses are treated as positive. Second, variables represented by capital letters are material constants, while variables represented by lower case letters are functions of other variables. Third, this section presents the model in an infinitesimal strain setting, but one can easily extended the model into the finite deformation realm using hypoelasticity.

The model additively decomposes the total strain rate $\dot{\varepsilon}$ into an elastic strain rate $\dot{\varepsilon}^{\text{el}}$, a thermal strain rate $\dot{\varepsilon}^{\text{th}}$, and a viscoplastic strain rate $\dot{\varepsilon}^{\text{vp}}$:

$$\dot{\varepsilon} = \dot{\varepsilon}^{\text{el}} + \dot{\varepsilon}^{\text{th}} + \dot{\varepsilon}^{\text{vp}}. \tag{1}$$

The elastic behavior utilizes generalized Hooke's law in rate form to relate $\dot{\varepsilon}^{\text{el}}$, the fourth-order isotropic elastic stiffness tensor $\mathbb{E}$, and the stress rate $\dot{\sigma}$:

$$\dot{\sigma} = \mathbb{E} : \dot{\varepsilon}^{\text{el}} = \mathbb{E} : \left(\dot{\varepsilon} - \dot{\varepsilon}^{\text{th}} - \dot{\varepsilon}^{\text{vp}} \right) \tag{2}$$

$$\mathbb{E} = (E_1 - \tfrac{2}{3} E_2) \boldsymbol{I} \otimes \boldsymbol{I} + 2 E_2 \mathbb{I}, \tag{3}$$

where E_1 is the bulk modulus, E_2 is the shear modulus, $\boldsymbol{I}$ is the second-order identity tensor, and $\mathbb{I}$ is the fourth-order symmetric identity tensor. The thermal strain portion of the model is simply

$$\dot{\varepsilon}^{\text{th}} = -A\,\dot{\theta}\,\boldsymbol{I} \tag{4}$$

where A is the coefficient of thermal expansion, and θ is the absolute temperature. The viscoplastic strain rate is additively decomposed into a pressure solution strain rate $\dot{\varepsilon}^{\text{ps}}$ and a dislocation glide strain rate $\dot{\varepsilon}^{\text{dg}}$

$$\dot{\varepsilon}^{\text{vp}} = \dot{\varepsilon}^{\text{ps}} + \dot{\varepsilon}^{\text{dg}}. \tag{5}$$

Pressure solution occurs along grain boundaries, while dislocation glide occurs inside grains, so the model assumes $\dot{\varepsilon}^{\text{ps}}$ and $\dot{\varepsilon}^{\text{dg}}$ are largely independent processes.

The $\dot{\varepsilon}^{\text{ps}}$ branch captures steady-state viscoplastic behavior at low stresses. This branch utilizes the following flow rule,

$$\dot{\varepsilon}^{\text{ps}} = \dot{\tilde{\varepsilon}}^{\text{ps}} \frac{\partial \tilde{\sigma}^{\text{ps}}}{\partial \boldsymbol{\sigma}}, \tag{6}$$

where $\dot{\tilde{\varepsilon}}^{\text{ps}}$ and $\tilde{\sigma}^{\text{ps}}$ are the equivalent pressure solution strain rate and stress, respectively. Pressure solution viscoplasticity is taken to be independent of the mean stress $\sigma^{\text{m}} = \text{tr}(\sigma)/3$ and driven entirely by the deviatoric stress σ^{dev}, so the pressure solution stress is simply

$$\sigma^{\text{ps}} = \sigma^{\text{dev}} = \sigma - \sigma^{\text{m}} \boldsymbol{I}. \tag{7}$$

This stress tensor is reduced to a scalar equivalent (von Mises) pressure solution stress as

$$\tilde{\sigma}^{\text{ps}} = \sqrt{\tfrac{3}{2} \sigma^{\text{ps}} : \sigma^{\text{ps}}}. \tag{8}$$

The equivalent pressure solution strain rate is given by

$$\dot{\tilde{\varepsilon}}^{\text{ps}} = P_1 \, \exp\left(-\frac{P_2}{\theta} \right) \frac{\tilde{\sigma}^{\text{ps}}}{\theta}, \tag{9}$$

where P_j are material constants (C. Spiers et al. 1990; Urai et al. 2008). Eq. (9) assumes any non-zero $\tilde{\sigma}^{\text{ps}}$ causes pressure solution flow, such that the pressure solution quasi-static (rate-independent) yield surface is simply a point at $\sigma = 0$.

The dislocation glide branch $\dot{\varepsilon}^{\text{dg}}$ dominates transient viscoplastic behavior at low stresses, and all viscoplastic behavior at medium to high stresses. Dislocation glide utilizes the following flow rule,

$$\dot{\varepsilon}^{\text{dg}} = \dot{\tilde{\varepsilon}}^{\text{dg}} \frac{\partial \tilde{\sigma}^{\text{dg}}}{\partial \boldsymbol{\sigma}}, \tag{10}$$

where $\dot{\tilde{\varepsilon}}^{\text{dg}}$ and $\tilde{\sigma}^{\text{dg}}$ are the equivalent dislocation glide strain rate and stress, respectively. In contrast to the pressure solution branch and the majority of other salt models, the model assumes dislocation glide is driven by a dislocation glide stress

$$\sigma^{\text{dg}} = \sigma^{\text{dev}} - \boldsymbol{b} \tag{11}$$

that includes $\boldsymbol{b}$, a second-order tensor called the back stress. With this definition for $\boldsymbol{\sigma}^{\mathrm{dg}}$, the equivalent (von Mises) dislocation glide stress is

$$\tilde{\sigma}^{\mathrm{dg}} = \sqrt{\tfrac{3}{2}\,\boldsymbol{\sigma}^{\mathrm{dg}} : \boldsymbol{\sigma}^{\mathrm{dg}}}. \tag{12}$$

Unlike the pressure solution branch, the dislocation glide branch has a finite size, quasi-static, yield surface, defined as

$$g = \tilde{\sigma}^{\mathrm{dg}} - G_0\, y, \tag{13}$$

where G_0 is a material constant and y is an isotropic hardening variable called the drag stress that evolves from a positive initial value Y_0 to some positive value. By default, $G_0 = E_2 \times 10^{-10}/Y_0$, which makes the $g = 0$ surface typically very small relative to $\tilde{\sigma}^{\mathrm{dg}}$. The equivalent dislocation glide strain rate is

$$\dot{\tilde{\varepsilon}}^{\mathrm{dg}} = \begin{cases} 0 & \text{for } g < 0 \\[2mm] G_1\,\exp\left(-\dfrac{G_2}{\theta}\right)\left[\sinh\left(\dfrac{\tilde{\sigma}^{\mathrm{dg}}}{y}\right)\right]^{G_3} & \text{for } g \geq 0 \end{cases}, \tag{14}$$

where G_j are material constants.

The drag stress y evolves according to

$$\dot{y} = Y_1\left(\frac{Y_1}{y}\right)^{Y_2}\left(1 - \frac{y}{\bar{y}}\right)\dot{\tilde{\varepsilon}}^{\mathrm{dg}}, \tag{15}$$

where

$$\bar{y} = \frac{\bar{\sigma} - \bar{b}}{\sinh^{-1}\left\{\left[\dfrac{\dot{\tilde{\varepsilon}}^{\mathrm{dg}}}{G_1\,\exp\left(-G_2/\theta\right)}\right]^{1/G_3}\right\}} \tag{16}$$

is the drag stress saturation,

$$\bar{\sigma} = Y_4\,\sinh^{-1}\left\{\left[\frac{\dot{\tilde{\varepsilon}}^{\mathrm{dg}}}{Y_3\,\exp\left(-G_2/\theta\right)}\right]^{1/Y_5}\right\} \tag{17}$$

is the equivalent (von Mises) stress saturation, $\bar{b}$ is the equivalent back stress saturation (discussed below), and Y_j are material parameters.

The back stress has a similar, yet different, set of evolution equations. Following Chaboche (1986), $\boldsymbol{b}$ is decomposed as

$$\boldsymbol{b} = \sum_{j=1}^{2} \boldsymbol{b}_j, \tag{18}$$

where $\boldsymbol{b}_1$ is a short range, quickly evolving, back stress and $\boldsymbol{b}_2$ is a long range, slowly evolving, back stress. Each back stress has an equivalent back stress defined as

$$\tilde{b}_j = \sqrt{\frac{3}{2}\,\boldsymbol{b}_j : \boldsymbol{b}_j}, \tag{19}$$

and each back stress begins at $\boldsymbol{B}_{j0}$, which must be deviatoric ($\mathrm{tr}(\boldsymbol{B}_{j0}) = 0$) and is set to the zero tensor $\boldsymbol{0}$ by default. As deformation proceeds, each back stress evolves according to

$$\dot{\boldsymbol{b}}_j = B_{j1}\left(\frac{2}{3}\,\dot{\boldsymbol{\varepsilon}}^{\mathrm{dg}} - \frac{\boldsymbol{b}_j}{\bar{b}_j}\,\dot{\tilde{\varepsilon}}^{\mathrm{dg}}\right), \tag{20}$$

where

$$\bar{b}_j = B_{j2}\, B_{j3}\, \tanh\left(\frac{\bar{\sigma}}{B_{j3}}\right) \tag{21}$$

is the jth equivalent back stress saturation and B_{jk} are material constants. Analogous to Eq. (18), the equivalent back stresses can be summed as

$$\tilde{b} = \sum_{j=1}^{2} \tilde{b}_j \qquad \text{and} \qquad \bar{b} = \sum_{j=1}^{2} \bar{b}_j. \tag{22}$$

All materials parameters should be non-negative to obtain typical material behavior. Furthermore, P_1, G_1, Y_1, Y_3, Y_4, Y_6, B_{j2}, B_{j3}, and $1 - \sum_{j=1}^{2} B_{j2}$ each must be non-negative to ensure y, $\bar{y}$, $\bar{b}_j$, $\bar{\sigma}$, $\dot{\tilde{\varepsilon}}^{\text{ps}}$, $\dot{\tilde{\varepsilon}}^{\text{dg}}$ are each non-negative.

3 Discussion of Formulation

This section briefly discusses some salient details of the model formulation. A more thorough discussion will be published at a later date.

3.1 Pressure Solution Branch

The pressure solution branch does not include any hardening (transient strain) for several reasons. According to a simple calculation, the increase in salt solubility in a brine film, of 0.1 μm thickness, surrounding a grain, of 10 mm size, due to a 1 MPa increase in $\tilde{\sigma}^{\text{ps}}$, at $\theta = 100\ ^\circ\text{C}$ would produce a negligible transient creep strain on the order of 10^{-8} (C. J. Spiers 2021). Pressure solution-based redistribution of grain boundary stresses, or other structural changes to grain boundaries, could perhaps create a hardening effect, but a succinct, quantitative, description of such effects is not known to the author. On the other hand, the existence of sub-grains corresponding to low stresses in in-situ deformed samples (Carter et al. 1993) and reverse creep at low stresses (Gharbi et al. 2020) suggest that dislocation glide is active during low stress creep, even if dislocation glide does not dominate the steady-state rate. It, therefore, seems reasonable to assume dislocation glide creep dominates transient creep at low stresses, while pressure solution creep dominates steady-state creep at low stresses.

3.2 Dislocation Glide Branch

Although the dislocation glide branch is largely phenomenological, some loose physical meaning can be attached to the back stresses and drag stress. The back stresses represent hardening due to heterogenously distributed dislocation substructures, such as sub-grains and wavy slip lines produced by dislocation climb and cross-slip, respectively (Carter et al. 1993). These substructures are commonly observed at low to medium strain rates (10^{-12} to 10^{-8} 1/s). The drag stress represents hardening due to more uniform dislocation distributions, as are observed at higher strain rates (Raj et al. 1989).

The motivation behind the name "drag stress" can be seen by inverting the $g \geq 0$ case in Eq. (14) as

$$\tilde{\sigma}^{\text{dg}} = y\, \sinh^{-1}\left\{\left[\frac{\dot{\tilde{\varepsilon}}^{\text{dg}}}{G_1\, \exp\left(-G_2/\theta\right)}\right]^{1/G_3}\right\}, \tag{23}$$

in which $\tilde{\sigma}^{\text{dg}}$ is equal to y multiplied by a non-linear function of $\dot{\tilde{\varepsilon}}^{\text{dg}}$. Thus, y plays a role similar to an evolving dashpot in rheological models.

Another important observation is the stresses σ^{dg}, and $\boldsymbol{b}$ are co-axial along proportional stress paths, such that Eqs. (11) and (12) can be simplified to

$$\tilde{\sigma} = \tilde{b} + \tilde{\sigma}^{dg}, \tag{24}$$

where $\tilde{\sigma} = \sqrt{\frac{3}{2}\,\sigma^{dev} : \sigma^{dev}}$. Eq. (24) can be seen as decomposing $\tilde{\sigma}$ into a back stress contribution $\tilde{b}$ and a drag stress contribution $\tilde{\sigma}^{dg}$ (see Eq. (23)) when $\dot{\tilde{\varepsilon}}^{dg}$ is controlled, as approximately occurs in a constant strain rate test.

Both hardening evolution equations (Eqs. (15) and (20)) conform to the Bailey-Orowan concept, in which the hardening rate is the result of a competition between a strain hardening term and a strain (a.k.a. dynamic) recovery term. Hardening saturates when the hardening and recovery rates balance one another ($\dot{y} = 0$ and $\dot{\boldsymbol{b}}_j = \boldsymbol{0}$). At hardening saturation, $\tilde{b}_j = \bar{b}_j$, $y = \bar{y}$, the stresses σ^{dg} and $\boldsymbol{b}$ are co-axial (even for non-proportional stress paths), such that Eqs. (14), (16), (17) and (24) combine to give $\tilde{\sigma} = \bar{\sigma}$. Inverting the expression for $\bar{\sigma}$ in Eq. (17) results in a steady-state dislocation glide strain rate of

$$\dot{\tilde{\varepsilon}}^{dg} = Y_3\,\exp\left(-\frac{G_2}{\theta}\right)\left[\sinh\left(\frac{\bar{\sigma}}{Y_4}\right)\right]^{Y_5}, \tag{25}$$

which was proposed by Garofalo (1963).

The saturation stress $\bar{\sigma}$ can be decomposed, similar to Eq. (24), as

$$\bar{\sigma} = \bar{b} + \bar{\sigma}^{dg}, \tag{26}$$

where $\bar{\sigma}^{dg} = \bar{y}\,\sinh^{-1}\left\{\left[\dot{\tilde{\varepsilon}}^{dg}/(G_1\,\exp(-G_2/\theta))\right]^{1/G_3}\right\}$. Clearly, one must decide how to partition the hardening between back stress and drag stress contributions. The hyperbolic tangent in Eq. (21) encourages one to make back stress contributions dominate at low stresses (low strain rates) and drag stress contributions dominate at high stresses (high strain rates). This important model assumption is based on direct measurements of the back stress in single phase metals (Takeuchi et al. 1976, Figure 15), as well as the microstructural observations at the start of this sub-section.

4   Calibration

This section reviews four model calibrations against a series of damage-free, axisymmetric compression, constant stress, and constant strain rate tests on salt from the Waste Isolation Pilot Plant (WIPP). Attention is focused on calibration performance rather than the calibration procedure.

The details of the axisymmetric compression tests on WIPP salt can be found in Salzer et al. (2015), Düsterloh et al. (2015), and Reedlunn (2016), but some details are reviewed herein. Each test began with a hydrostatic consolidation stage for one to ten days at 20 MPa of pressure. The axial logarithmic strain at the end of the consolidation stage is denoted as $\varepsilon_{zz}(t_0)$, and $\varepsilon_{zz} - \varepsilon_{zz}(t_0)$ is the change in strain thereafter. In the constant strain rate tests, the axial engineering strain rate $\dot{e}_{zz}$ was held fixed, not the axial logarithmic strain rate $\dot{\varepsilon}_{zz} = \dot{e}_{zz}/(1 - e_{zz})$, so care was taken to convert between the two strain rate measures as needed. After the consolidation stage, the radial confining pressure was held at $\sigma_{rr} = 10$ or 20 MPa to avoid significant micro-cracking.

Several calibration decisions were made in the absence of recent experimental data on WIPP salt. (1) The thermoelastic parameters in Table 1 were inherited from Munson et al. (1989). (2) The parameter G_1 was set to 10^9 1/s. (3) The parameter P_2 was assumed to be

(a) Steady-state viscoplastic strain rate

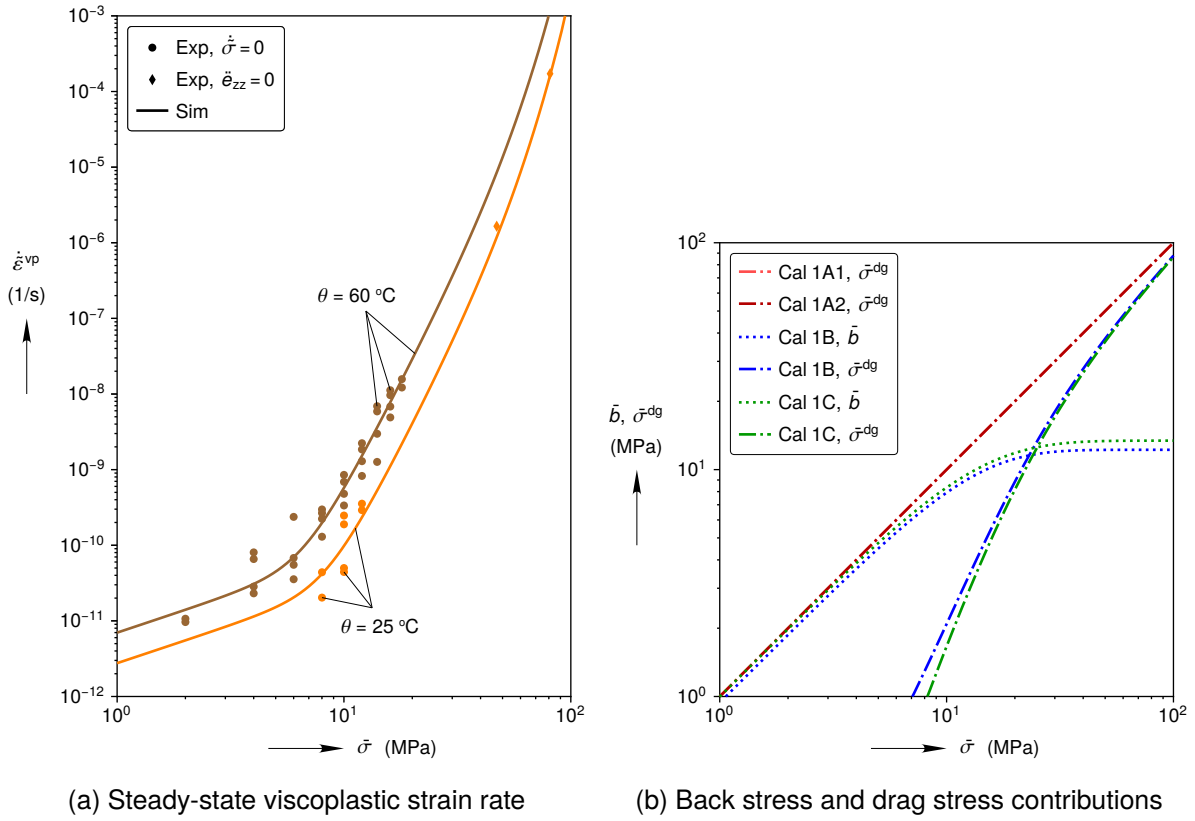(b) Back stress and drag stress contributions

Figure 1: Behavior at hardening saturation.

2950 K, based on the granular salt compaction experiments in C. Spiers et al. (1990). (4) The calibrations focused on the $20 \leq \theta \leq 60\,°C$ temperature range.

All four model calibrations utilized the same steady-state viscoplastic strain rate calibration. The constant stress experiments provided saturation strain rate measurements for stresses ranging from 2 to 18 MPa, but two constant strain rate experiments provided saturation stress measurements at higher stresses of 47 and 81 MPa at $\theta = 25\,°C$, as shown in Fig. 1a. The strain rate saturation parameters P_1, G_2, Y_3, Y_4, and Y_5 were optimized, in a least squares sense, against the strain rate measurements. The resulting fits are shown in Fig. 1a and the parameter values are listed in Table 1. Figure 1a also shows that the constant stress and constant strain rate experiments did not overlap at hardening saturation, which made calibrating the hardening parameters challenging.

The hardening parameters were fit against the strain vs. time curves from the first stage of the constant stress tests and the stress vs. strain curves from the damage-free portions of the constant strain rate tests. The fitting process minimized a merit function that compared simulations against experimental measurements in an integrated least-squares sense. The resulting parameter sets are listed in Table 1. The performance of each hardening calibration is shown in Figs. 2 and 3. Figure 2a depicts the transient creep strain $\tilde{\varepsilon}^{\mathrm{tr}}(t_1)$ after $t_1 \approx 50$ days of creep at various applied stresses and two temperatures. (The transient strain $\tilde{\varepsilon}^{\mathrm{tr}} = \tilde{\varepsilon}^{\mathrm{tr}}(t)$ is ε_{zz} minus the accumulated elastic and steady-state creep strain.) Fig. 2b depicts the characteristic creep time t^{ch}, which is the time for $\tilde{\varepsilon}^{\mathrm{tr}}$ to reach $0.8\,\tilde{\varepsilon}^{\mathrm{tr}}(t_1)$. Each simulated curve in Fig. 2 came from analyzing the results of 100 simulations in the same manner as the experiments. The plots in Fig. 3 show the stress vs. strain curves for constant strain rate experiments and simulations at three different engineering strain rates.

(a) Transient creep strain at $t_1 \approx 50$ d
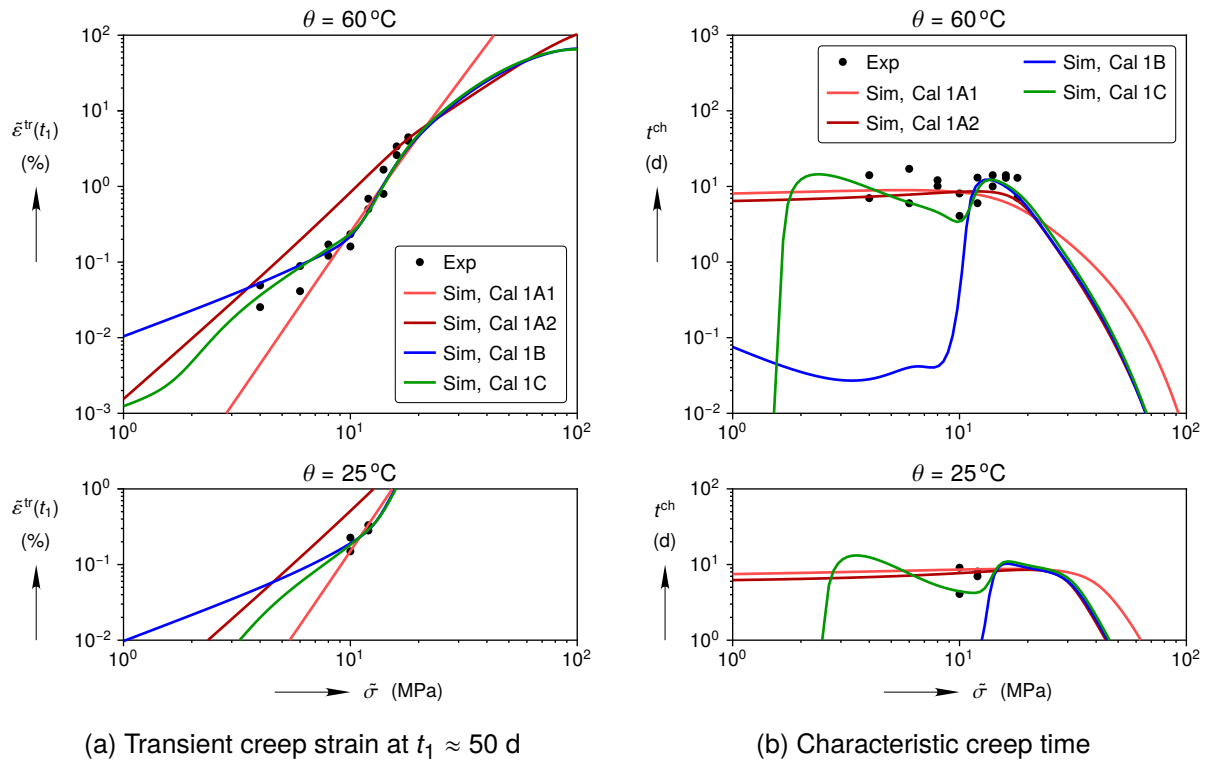
(b) Characteristic creep time

Figure 2: Transient strains and characteristic times from constant stress (first creep stage only) simulations compared against experimental measurements.
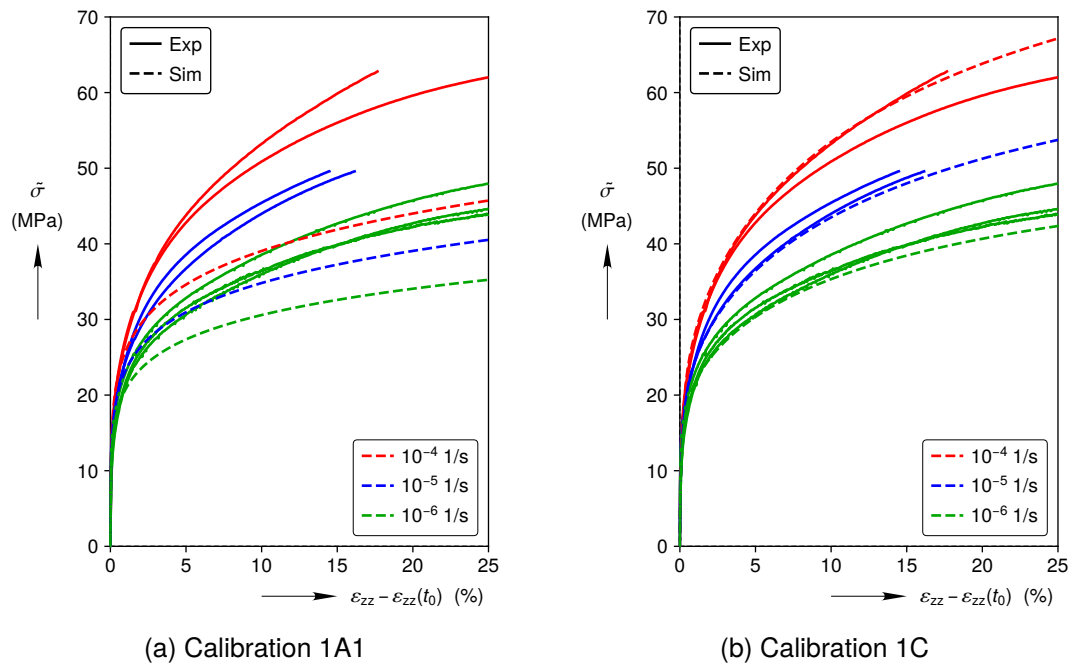

(a) Calibration 1A1

(b) Calibration 1C

Figure 3: Results from room temperature constant strain rate simulations from Calibration 1A1 and 1C compared against experimental measurements. (Constant strain rate simulation results for Calibrations 1A2 and 1B were similar to the Calibration 1C results in (b).)

Calibration 1A1 optimized G_3, Y_1, and Y_2 against the first-stage constant stress tests with $10 \leq \tilde{\sigma} \leq 18$ MPa. The Calibration 1A1 simulations of constant stress tests produce $\tilde{\varepsilon}^{\text{tr}}(t_1)$ and t^{ch} values that agree with the experimental measurements (see Figs. 2a and 2b) within the calibration range, but not outside the calibration range. The constant stress simulations at $\tilde{\sigma} \leq 6$ MPa under-predict the $\tilde{\varepsilon}^{\text{tr}}(t_1)$ values (see Fig. 2a), and the constant strain rate simulations substantially under-predict the stresses for $\varepsilon_{zz} - \varepsilon_{zz}(t_0) > 1$ % at all three strain rates (see Fig. 3a). This latter under-prediction is especially problematic because a model that cannot capture damage-free constant strain rate behavior cannot be used to infer the degree of damage in low confining pressure constant strain rate tests.

Table 1: Calibrations (All calibrations utilize the default values of $G_0 = E_2 \times 10^{-10}/Y_0$ and $\boldsymbol{B}_{j0} = \boldsymbol{0}$.)

Type	Parameter	Units	Cal 1A1	Cal 1A2	Cal 1B	Cal 1C
Thermo-elastic	E_1	Pa	20.67×10^9	20.67×10^9	20.67×10^9	20.67×10^9
	E_2	Pa	12.40×10^9	12.40×10^9	12.40×10^9	12.40×10^9
	A	1/K	45×10^{-6}	45×10^{-6}	45×10^{-6}	45×10^{-6}
Pressure Solution	P_1	K/(Pa s)	16.39×10^{-12}	16.39×10^{-12}	16.39×10^{-12}	16.39×10^{-12}
	P_2	K	2.950×10^3	2.950×10^3	2.950×10^3	2.950×10^3
Dislocation Glide	G_1	1/s	1×10^9	1×10^9	1×10^9	1×10^9
	G_2	K	5.585×10^3	5.585×10^3	5.585×10^3	5.585×10^3
	G_3	–	22.03	14.12	8.543	7.973
	Y_0	Pa	100×10^3	100×10^3	100×10^3	100×10^3
	Y_1	Pa	86.08×10^6	221.6×10^6	451.6×10^6	496.7×10^6
	Y_2	–	4.240	2.138	1.035	0.9911
	Y_3	1/s	36.00	36.00	36.00	36.00
	Y_4	Pa	43.50×10^6	43.50×10^6	43.50×10^6	43.50×10^6
	Y_5	–	5.623	5.623	5.623	5.623
	B_{11}	Pa	0	0	0	84.63×10^9
	B_{12}	–	1×10^{-9}	1×10^{-9}	1×10^{-9}	0.2910
	B_{13}	Pa	1×10^9	1×10^9	1×10^9	18.60×10^6
	B_{21}	Pa	0	0	8.303×10^9	5.445×10^9
	B_{22}	–	1×10^{-9}	1×10^{-9}	0.9420	0.7090
	B_{23}	Pa	1×10^9	1×10^9	12.98×10^6	11.29×10^6

Calibration 1A2, by contrast, optimized G_3, Y_1, and Y_2 against the constant strain rate tests with $10^{-6} \leq \dot{e}_{zz} \leq 10^{-4}$ 1/s. The back stress evolution rates were again set to zero ($B_{j1} = 0$). The Calibration 1A2 simulations produced stress–strain responses similar to the Calibration 1C responses shown in Fig. 3b as desired, but simulations of the constant stress tests at $\tilde{\sigma} < 16$ MPa substantially over-predicted $\tilde{\varepsilon}^{\text{tr}}(t_1)$ (see Fig. 2a).

Calibration 1B fit G_3, Y_1, Y_2, B_{21}, B_{22}, and B_{23} against the first-stage constant stress tests with $10 \leq \tilde{\sigma} \leq 18$ MPa and the constant strain rate tests with $10^{-6} \leq \dot{e}_{zz} \leq 10^{-4}$ 1/s. The short range back stress evolution rate was set to zero ($B_{11} = 0$). Calibration 1B captured the measured $\tilde{\varepsilon}^{\text{tr}}(t_1)$ and t^{ch} values for $10 \leq \tilde{\sigma} \leq 18$ MPa (see Figs. 2a and 2b), and the Calibration 1B stress-strain curves were similar to the Calibration 1C curves (see Fig. 3b). Outside of the calibration range, Calibration 1B reasonably predicted the $\tilde{\varepsilon}^{\text{tr}}(t_1)$ values for $4 \leq \tilde{\sigma} \leq 8$ MPa, but under-predicted the t^{ch} measurements by roughly $100\times$ in the same stress range.

Calibration 1C fit G_3, Y_1, Y_2, B_{11}, B_{13}, B_{21}, B_{22}, and B_{23} against the first-stage constant stress tests with $4 \leq \tilde{\sigma} \leq 18$ MPa and the constant strain rate tests with $10^{-6} \leq \dot{e}_{zz} \leq 10^{-4}$ 1/s. Preliminary optimizations that allowed both B_{12} and B_{22} to vary produced $B_{12} + B_{22} \approx 0.999$

(recall $B_{12}+B_{22} > 1$ is prohibited), so $B_{12} = 1-B_{22}$ was simply enforced for the final Calibration 1C optimization. This most flexible model calibration produced behaviors similar to Calibration 1B, except it more accurately captured the t^{ch} measurements at $4 \leq \tilde{\sigma} \leq 8$ MPa (see Fig. 2b).

The relative contributions of the back stresses and drag stress at hardening saturation can be seen in Fig. 1b. Calibrations 1A1 and 1A2 do not include back stresses, so the drag stress contribution $\bar{\sigma}^{dg}$ dominates at all applied stresses and strain rates. Calibrations 1B and 1C, however, conform to the discussion at the end of Section 3.2: $\bar{b}$ dominates at low stresses and $\bar{\sigma}^{dg}$ dominates at high stresses.

5 Validation

The previous section demonstrated how the drag stress and two back stresses can be used to capture salt's damage-free behavior at different stresses and strain rates. All the calibration experiments, however, involved monotonic proportional stress paths. This section compares Calibrations 1A2, 1B, and 1C against a constant strain rate experiment with a non-monotonic proportional stress path, which leads to the Bauschinger effect.
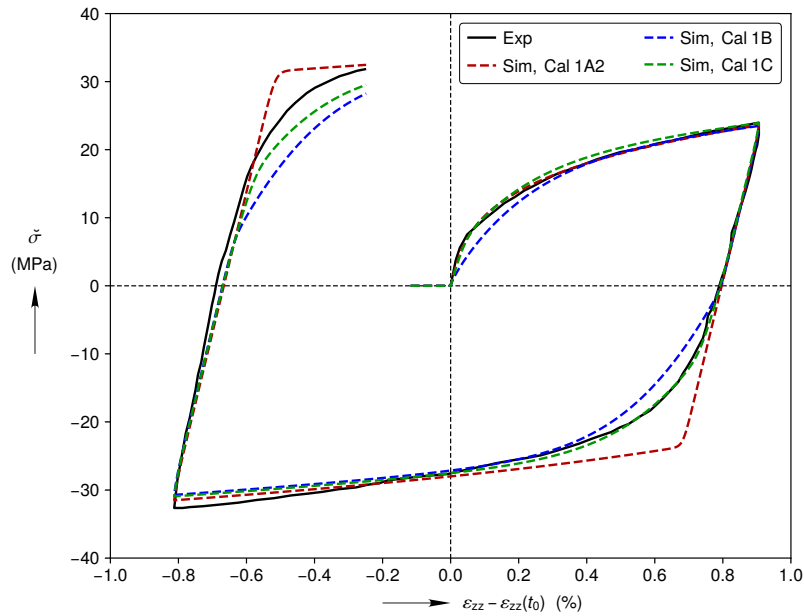

Figure 4: A comparison of three different model calibration stress–strain responses against experimental measurements on artificial rock salt.

The Bauschinger effect has not been studied on WIPP salt, so an experiment on artificial rock salt (Aubertin, Julien, et al. 1999, Fig. 5d) was utilized instead. Fig. 4 displays the artificial rock salt stress–strain response at $|\dot{\varepsilon}_{zz}| = 3.5 \times 10^{-5}$ 1/s, $\sigma_{rr} = 53$ MPa, and $\theta = 20$ °C, during three stages: axisymmetric compression, axisymmetric extension, and a second axisymmetric compression stage[*]. This artificial rock salt experiment was simulated using slightly modified versions of Calibration 1A2, 1B, and 1C. The elastic modui E_1 and E_2 were each reduced by a factor of 22.5/31.0 = 0.7258 to properly capture the artificial rock salt's linear elastic behavior, as reported by Aubertin, Yahya, et al. (1999). In addition, the simulated stress difference $\breve{\sigma}$ =

---

[*]To enhance legibility, brief elastic unloading and reloading stages in the actual experiment were omitted, and the measured stress and strain were each multiplied by –1 to cause the first stage to be axisymmetric compression rather than axisymmetric extension.

$\sigma_{zz} - \sigma_{rr}$ values were scaled by 0.92× to bring the WIPP salt derived predictions more in-line with the artificial salt measurements during the first axisymmetric compression stage.

Fig. 4 also compares the simulated stress–strain responses against the experimental measurements. The (scaled) $\breve{\sigma}$ from Calibration 1A2, which includes only drag stress hardening, matches the experimental measurements nearly exactly during the first axisymmetric compression stage, but fails to capture the Bauschinger effect during the axisymmetric extension and second axisymmetric compression stages. Adding one back stress in Calibration 1B produces a prediction that qualitatively represents the Bauschinger effect, but the prediction is not quite stiff enough at the onset of hardening and re-hardening. Adding a second kinematic hardening back stress causes Calibration 1C to accurately represent the initial hardening during the first axisymmetric compression stage, accurately *predict* the re-hardening during the axisymmetric extension stage, and come closer to predicting the re-hardening during the second axisymmetric compression stage.

This prediction of the Bauschinger effect is significant because the Calibration 1C back stress was not calibrated against tests with non-monotonic loading, as is often done. Instead, the back stress parameters B_{ij} were calibrated against monotonic loading tests, such that the back stress dominated at low strain rates (low stresses) and played a lesser role in at high strain rates (high stresses) (see Fig. 1b). The back stress contribution at a high strain rate of $|\dot{\varepsilon}_{zz}| = 3.5 \times 10^{-5}$ 1/s is still significant, though, as shown by the difference between the simulation results in Fig. 4. The successful prediction of the Bauschinger effect by Calibration 1C, therefore, validates the hyperbolic tangent in Eq. (21).

Although not shown herein, the model can also represent reverse creep during a multi-stage constant stress experiment. During forward creep at an applied $\tilde{\sigma}$, $\tilde{b}$ evolves to some value $\tilde{b} < \tilde{\sigma}$. Subsequently decreasing $\tilde{\sigma}$ to $\tilde{\sigma} < \tilde{b}$ produces reverse creep (see Eq. (10)).

6   Summary

A new model for the thermo-viscoplastic behavior of damage-free rock salt has been developed, calibrated, and partially validated. The pressure solution branch captured salt's steady-state behavior at low stresses. The dislocation glide branch captured salt's transient behavior at low stresses, and all viscoplastic behavior at medium to high stresses. After calibrating the model against monotonic experiments, the model successfully predicted the Bauschinger effect in a non-monotonic experiment. This result validates a key assumption in the model: the back stress dominates at low strain rates (low stresses) and the drag stress dominates at high strain rates (high stresses). Future work will likely focus on adding damage and healing to the model.

Acknowledgements

References

AUBERTIN, M., JULIEN, M. R., SERVANT, S., and GILL, D. E. (1999). A rate-dependent model for the ductile behavior of salt rocks. Canadian Geotechnical Journal, 36, 4, 660–674.

AUBERTIN, M., YAHYA, O. M. L., and JULIEN, M. (1999). Modeling mixed hardening of alkali halides with a modified version of an internal state variables model. International Journal of Plasticity, 15, 10, 1067–1088.

CARTER, N., HORSEMAN, S., RUSSELL, J., and HANDIN, J. (1993). Rheology of rocksalt. Journal of Structural Geology, 15, 9-10, 1257–1271.

CHABOCHE, J.-L. (1986). Time-independent constitutive theories for cyclic plasticity. International Journal of plasticity, 2, 2, 149–188.

DÜSTERLOH, U., HERCHEN, K., LUX, K.-H., SALZER, K., GÜNTHER, R.-M., MINKLEY, W., HAMPEL, A., ARGÜELLO JR, J. G., and HANSEN, F. D. (2015). Joint Project III on the comparison of constitutive models for the thermomechanical behavior of rock salt. III. Extensive laboratory test program with argillaceous salt from WIPP and comparison of test results. Proc. 8th Conference on the Mechanical Behavior of Salt, 13–21.

GAROFALO, F. (1963). An empirical relation defining the stress dependence of minimum creep rate in metals. Trans. AIME, 227, 351–356.

GHARBI, H., BÉREST, P., BLANCO-MARTÍN, L., and BROUARD, B. (Oct. 2020). Determining upper and lower bounds for steady state strain rate during a creep test on a salt sample. International Journal of Rock Mechanics and Mining Sciences, 134, 104452.

MUNSON, D. E., FOSSUM, A. F., and SENSENY, P. E. (1989). Advances in resolution of discrepancies between predicted and measured in situ WIPP room closures. Tech. rep. SAND88-2948, Albuquerque, NM, USA: Sandia National Laboratories.

RAJ, S. V. and PHARR, G. (1989). Creep substructure formation in sodium chloride single crystals in the power law and exponential creep regimes. Materials Science and Engineering: A, 122, 2, 233–242.

REEDLUNN, B. (2016). Reinvestigation into closure predictions of Room D at the Waste Isolation Pilot Plant. Tech. rep. SAND2016-9961, Albuquerque, NM, USA: Sandia National Laboratories. DOI: 10.2172/1333709.

REEDLUNN, B. (Nov. 2018). Enhancements to the Munson-Dawson model for rock salt. Tech. rep. SAND2018-12601, Albuquerque, NM, USA: Sandia National Laboratories. DOI: 10.2172/1481508.

SALZER, K., GÜNTHER, R.-M., MINKLEY, W., NAUMANN, D., POPP, T., HAMPEL, A., LUX, K.-H., HERCHEN, K., DÜSTERLOH, U., ARGÜELLO JR, J. G., and HANSEN, F. D. (2015). Joint Project III on the comparison of constitutive models for the thermomechanical behavior of rock salt. II. Extensive laboratory test program with clean salt from WIPP. Proc. 8th Conference on the Mechanical Behavior of Salt, 3–12.

SPIERS, C. J. (2021). Negligible transient strain due to pressure solution. Personal Communication.

SPIERS, C., SCHUTJENS, P., BRZESOWSKY, R., PEACH, C., LIEZENBERG, J., and ZWART, H. (1990). Experimental determination of constitutive parameters governing creep of rocksalt by pressure solution. Geological Society, London, Special Publications, 54, 1, 215–227.

TAKEUCHI, S. and ARGON, A. (1976). Steady-state creep of single-phase crystalline matter at high temperature. Journal of Materials Science, 11, 8, 1542–1566.

URAI, J., SCHLÉDER, Z., SPIERS, C., and KUKLA, P. (2008). Dynamics of complex intracontinental basins: The central European basin system. Springer-Verlag Berlin, Heidelberg. Chap. 5.2: Flow and transport properties of salt rocks, 277–290.